Self-Compensation in Transparent Conducting F-doped SnO_2 - Supporting Information

Jack E. N. Swallow,[†] Ben Williamson,[‡,¶] Thomas J. Whittles,[†] Max Birkett,[†] Thomas J. Featherstone,[†] Nianhua Peng,[§] Alex Abbott,[‖] Mark Farnworth,[‖] Kieron J. Cheetham,[‖] Paul Warren,[‖] David O. Scanlon,[‡,¶,⊥] Vin R. Dhanak,[†] and Tim D. Veal[*,†]

†*Stephenson Institute for Renewable Energy and Department of Physics, University of Liverpool, Liverpool L69 7ZF, United Kingdom*

‡*Department of Chemistry, University College London, Kathleen Lonsdale Materials Chemistry, 20 Gordon Street, London WC1H 0AJ, United Kingdom*

¶*Thomas Young Centre, University College London, Gower Street, London WC1E 6BT, United Kingdom*

§*Surrey Ion Beam Centre, University of Surrey, Surrey GU2 7XH, United Kingdom*

‖*NSG Group, European Technical Centre, Hall Lane, Lathom, Ormskirk, Lancashire, L40 5UF, United Kingdom*

⊥*Diamond Light Source Ltd., Diamond House, Harwell Science and Innovation Campus, Didcot, Oxfordshire OX11 0DE, UK*

E-mail: T.Veal@liverpool.ac.uk

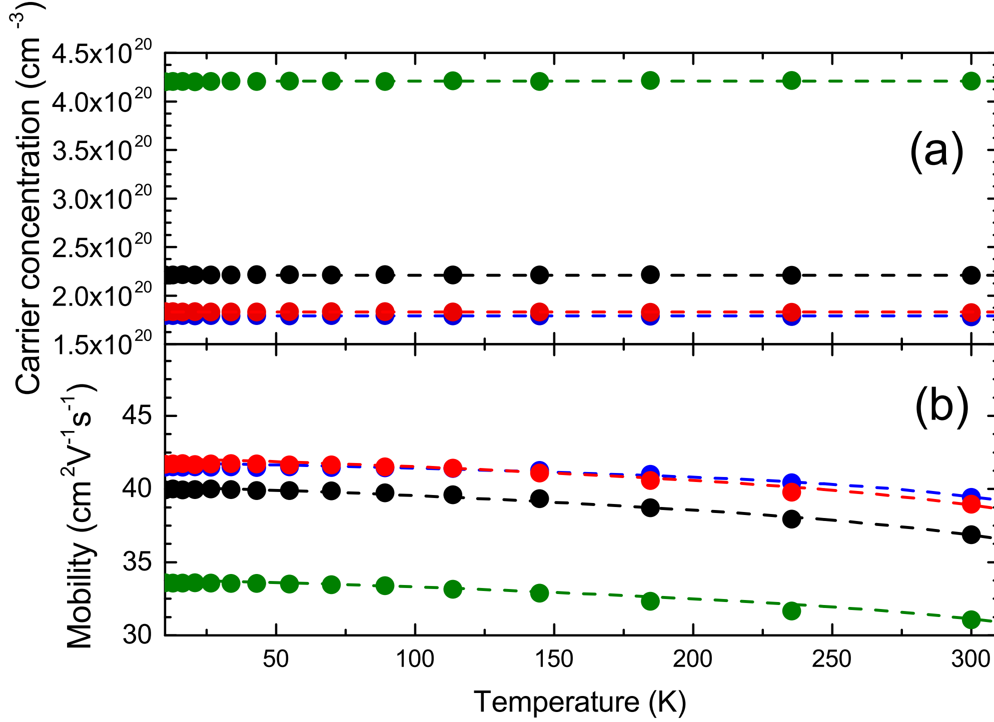

Figure S1: Temperature dependent carrier transport determined via Hall effect. (a) Carrier concentration as a function of temperature in the range of 10-300K. (b) Free carrier mobility as a function of temperature.

Temperature dependent Hall effect

For degenerately doped systems we do not expect carrier concentration to vary with temperature due to all carriers being ionized in the temperature range recorded. This is supported in the figure, a straight line has been plotted with the data to act as a guide for the eye. The same transport model from the full text, which accounts for ionized impurity scattering, acoustic deformation potential, longitudinal polar-optic phonons and grain boundary scattering has been plotted in (b). Ionized impurity scattering is the dominant scattering mechanism as expected, and does not vary with temperature because all carriers are ionized at all temperatures. After ∼125K the effect of longitudinal polar optical carrier scattering becomes much more important than at low temperatures which is evident in the downward curvature of the simulation lines.

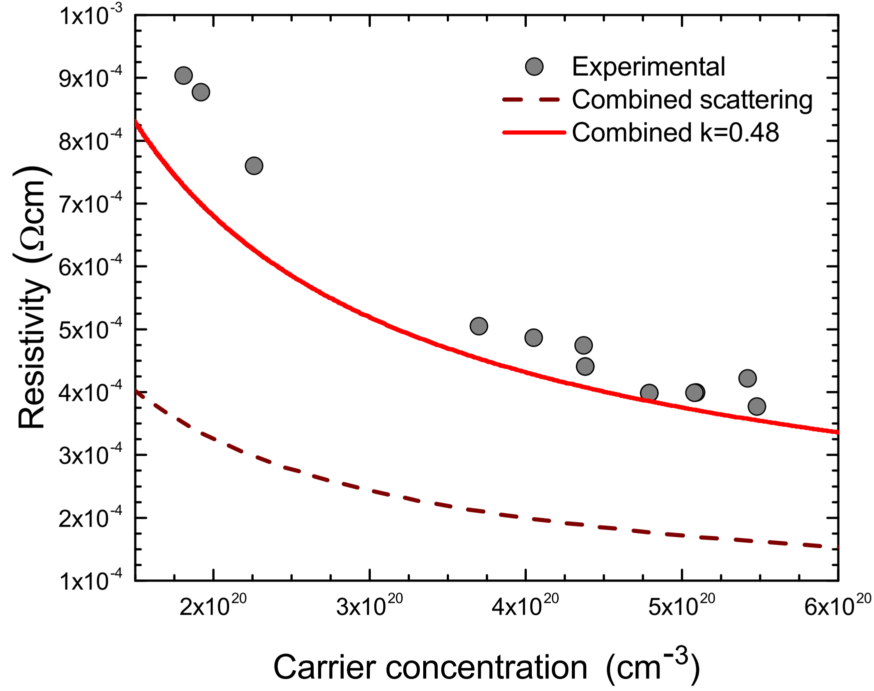

Figure S2: Transport data and simulation of resistivity and carrier density as determined via Hall effect and SIMS. The uncompensated model is shown as a dashed curved whilst the compensated (K=0.48) curve is solid.

Resistivity as a function of carrier concentration

Resistivity can be determined from carrier density (Via either Hall effect or SIMS) and mobility (obtained via Hall effect) measurements by $\rho = \frac{1}{ne\mu}$. Using both the data points and model curves from the full text we plot resistivity as a function of carrier concentration seen in figure S2. The combined scattering curve (brown dashed curve) is determined via Matthiessen's rule, combining the main scattering mechanisms present for degenerate FTO, i.e. ionized impurities, grain boundaries and phonon effects. This represents the theoretical minimum resistivity possible for FTO. The solid red curve displays the compensated curve fitted to the data. The compensated curve accounts for the effects of compensating acceptor defects determined to be due to the fluorine interstitial. These defects limit the mobility at a given carrier concentration negating the effects of heavy dopant incorporation.

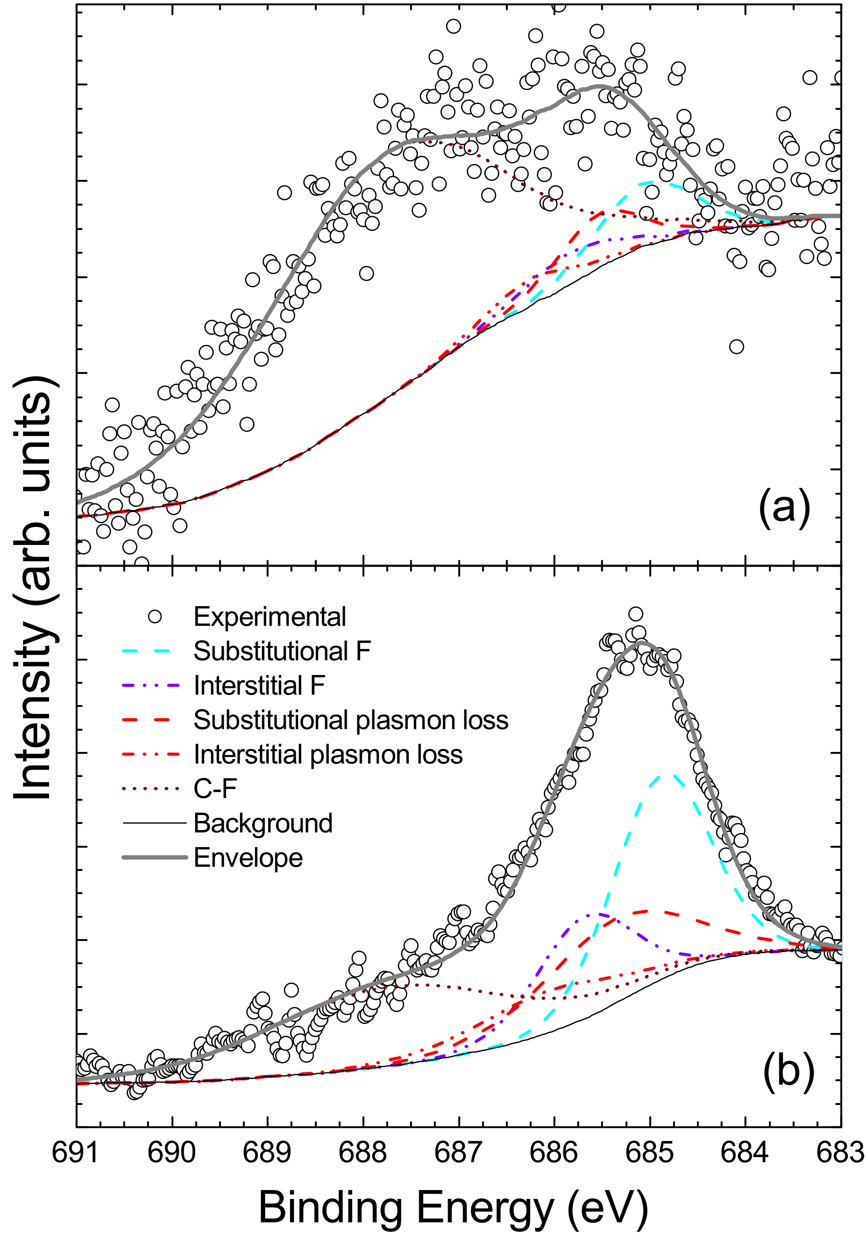

Figure S3: (a) XPS spectra for the F1s core level of FTO (n= $4.27 \times 10^{20}\text{cm}^{-3}$) measured as entered (b) XPS spectra for F1s core level after Ar^{+} ion bombardment surface treatment.

XPS spectra of F 1*s* as-entered

A comparison between the as-entered sample where no Ar^{+} ion bombardment had been performed prior to measuring, and the same sample subsequent to surface treatment. The four peaks associated with the substitutional and interstitial fluorine and their respective plasmon losses are seen as well as a large high binding energy component attributed to surface

contamination.[1–3] We do not expect there to be an associated plasmon loss component with the carbon contaminant due to it residing at the surface of the material, and so photoelectrons from the contaminant will not come into contact with the bulk free electron gas when being liberated from the material.

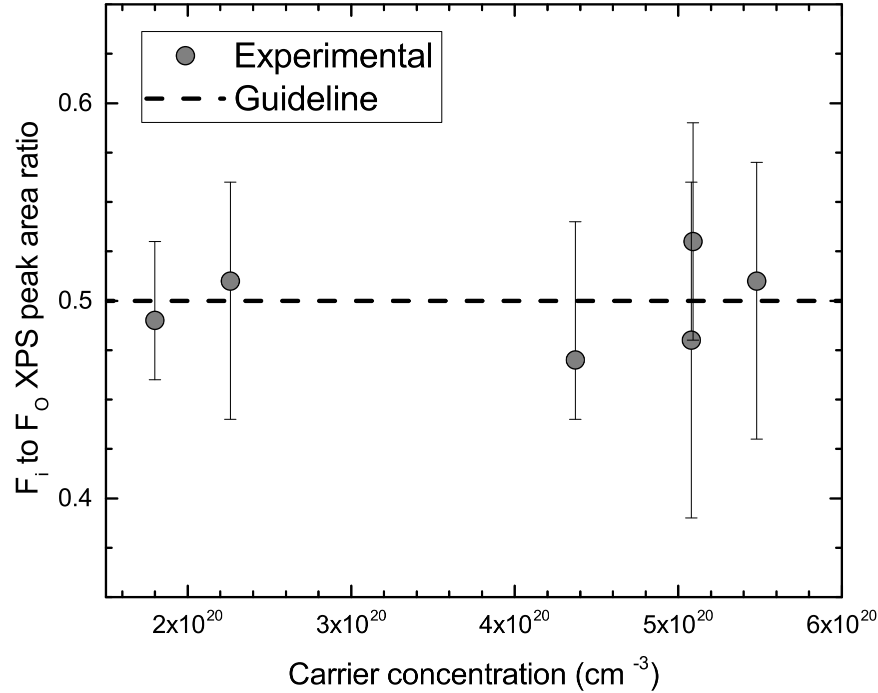

Figure S4: Ratio of interstitial to substitutional F as a function of free carrier concentration for a number of FTO samples as determined using XPS and Hall effect.

Interstitial to substitutional F ratio as a function of carrier concentration

XPS measurements were used to determine the ratio of interstitial to substitutional F. Hall effect was used to measure the carrier concentration of each sample. The ratio values all lie in the range 0.47 to 0.53. A dashed trend line has also been plotted at a ratio of 0.50, as a guide to the eye. Uncertainties were determined by varying the area fit parameter of the Gaussian-Lorentzian curves fitted for each of the data sets until the fit became clearly unphysical, which became the upper/lower bounds of the uncertainty.

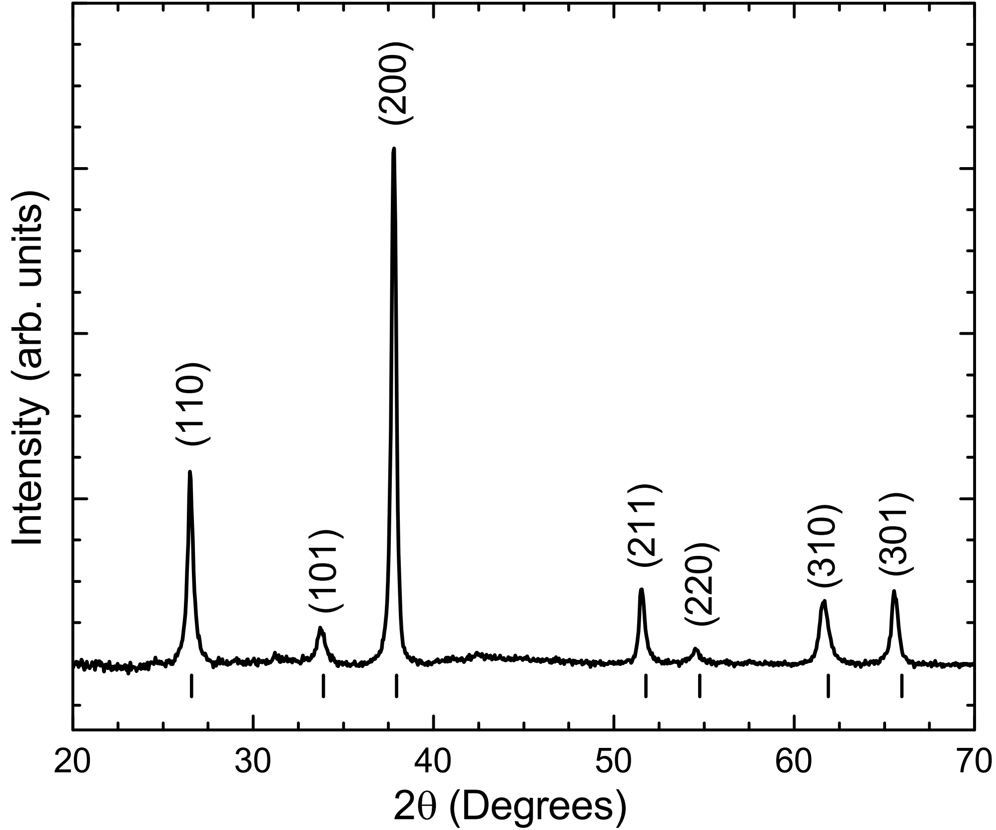

Figure S5: X-ray diffraction pattern of a typical FTO film.

X-ray diffraction of FTO

In order to confirm the structure of our FTO samples we performed XRD measurements using a PANalytical X'pert diffractometer. Figure S5 shows a typical diffraction pattern obtained. The prominent peak positions are labeled with the corresponding Miller indices, and peak positions determined from previous SnO_2 crystal structure data[4,5] (drawn as vertical lines underneath the peaks). A background subtraction has been performed in order to allow for easier comparison of the literature and measured peak positions. A number of indices are omitted from the plot as their intensities are below the background level so cannot be seen. The XRD patterns match well with those found in the literature.[6–9] It is clear that these CVD deposited FTO films are polycrystalline structure, with preferential (200) orientation. No unwanted impurity phases could be distinguished from the data with only peaks related to rutile SnO_2 being present.

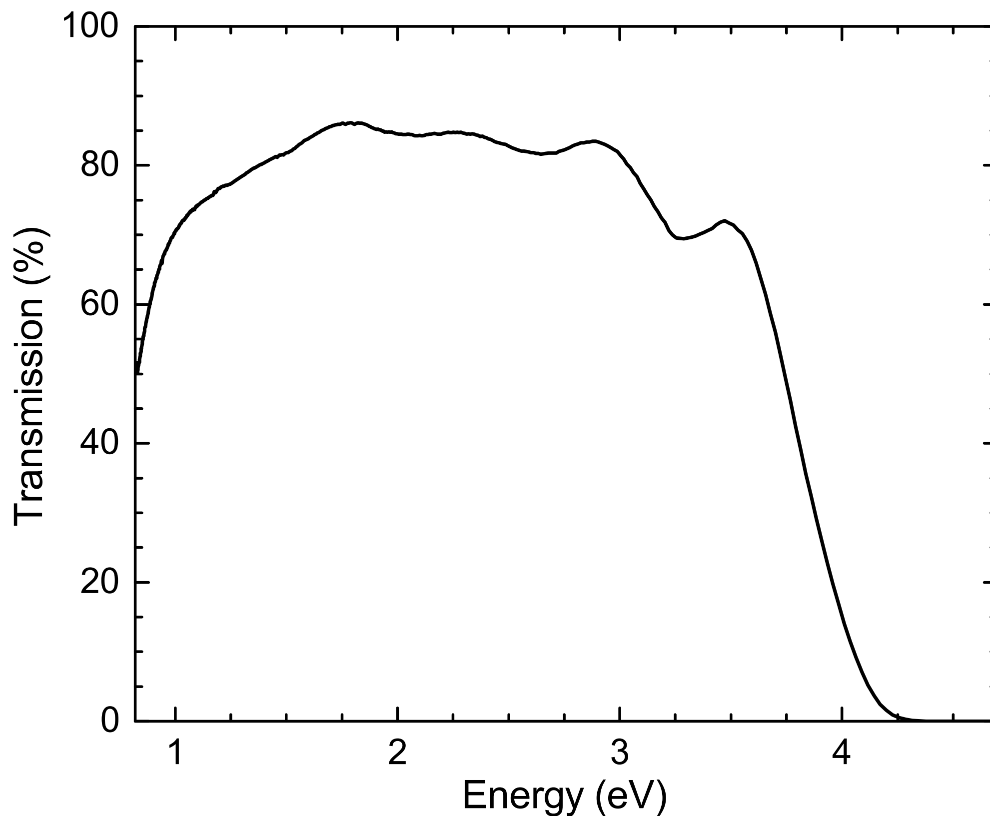

Figure S6: UV-Vis-NIR transmission spectra of a typical FTO sample.

Transmission of FTO

Figure S6 shows a transmission spectra for a typical FTO sample (n= 4.27×10^{20} cm^{-3}) measured using the Shimadzu UV-Vis-IR 3700 spectrophotometer over a range of ~0.75–4.75 eV. This plot corresponds to the absorption spectrum seen in the inset to Figure 3 in the main document. Transmission at $\lambda = 550$ nm (2.25 eV) is 84.8% and an average transmission of $\sim$ 80% is obtained for a wavelength range of 350–1250 nm (around 1–3.5 eV). These films demonstrate good optical properties across the visible and near ultraviolet spectrum.

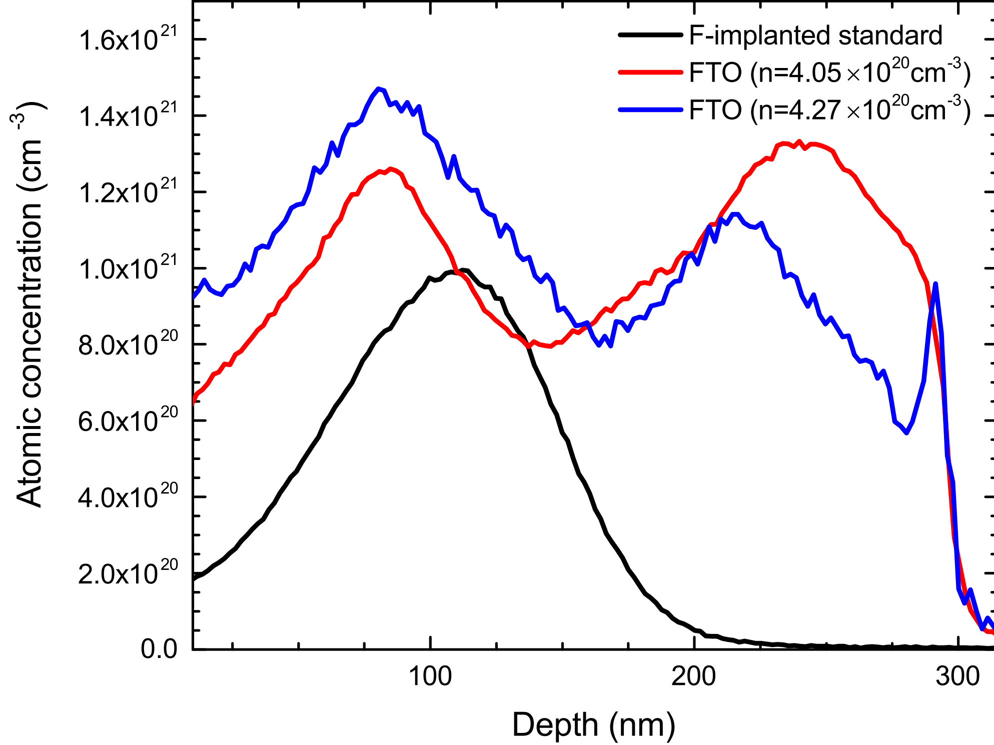

Figure S7: Calibrated secondary ion mass spectrometry (SIMS) data of the atomic fluorine signal from a typical FTO sample ($n_{Hall} = 4.05 \times 10^{20}$ cm^{-3} and $n_{Hall} = 4.27 \times 10^{20}$ cm^{-3} corresponding to the XPS data in the main manuscript) and a fluorine-implanted standard (1×10^{16} cm^{-2}). The x and y-axes have been calibrated to depth (nm) and concentration (cm^{-3}) respectively.

SIMS of FTO

Nominally undoped conducting SnO_2 was implanted with fluorine ions at 100 keV and fluences of 1×10^{16}, 5×10^{15}, and 1×10^{15} cm^{-2} at Surrey Ion Beam Centre. Time of flight (ToF) SIMS measurements were made, using the IonTof TOF-SIMS 5 instrument, of these implanted films and typical F-doped SnO_2 film with $n_{Hall} = 4.05 \times 10^{20}$ cm^{-3} and $n_{Hall} = 4.27 \times 10^{20}$ cm^{-3} (corresponding to the doping density of the sample in the XPS data in the main manuscript). Pulsed Bi^{3+} analysis ions were used to bombard the sample surface while a 1 keV Cs source was used as the sputtering beam. Analysis was performed on a 50.8×50.8 μm^2 sputter area. The CsF_2^+ ion intensity versus erosion time were converted to fluorine concentration versus depth. The y-axis in Figure S7 was scaled so that the area under the curve corresponding to the fluorine ion implanted film is 1×10^{16} cm^{-2}. This enabled the

fluorine concentration as a function of depth to be determined. The fluorine content varies significantly with depth as a result of the chemical vapour deposition process in on-line coating of float glass. The presented samples have an average fluorine concentration of [F] = $(1.08\pm0.11) \times 10^{21}$ cm^{-3} and [F] = $(1.06\pm0.11) \times 10^{21}$ cm^{-3}. The uncertainty is estimated by considering the uncertainties in the thicknesses obtained from profilometry (±25 nm), the implantation doses (±2%) and the possible matrix effects due to F concentrations in excess of 1 atomic %.

Table S1: Experimentally determined binding energy positions of F 1s peak components for F-doped SnO_2 and F-doped TiO_2. The data presented is from a number of sources which use different methods of calibrating the binding energy scale. Hence, the energy difference between F 1s components is also presented for comparison.

Material	Main component (eV)	Shoulder component (eV)	ΔE (eV)	Ref.
F:SnO_2	684.9	685.7	0.8	This work
F:SnO_2	684.7	685.7	1.0	10
F:SnO_2	685.7	687.3	1.6	11
F:SnO_2	684.7	687.5	2.8	12
F:SnO_2	685.1	-	-	13
F:SnO_2	684.4	-	-	14
F:TiO_2	684.9	686.4	1.5	15
F:TiO_2	683.6	684.7	1.1	16
F:TiO_2	684.3	685.4	1.1	17
F:TiO_2	684.1	685.3	1.2	18

Binding energies for F 1*s* region of F-doped SnO_2 and F-doped TiO_2

XPS binding energy values for the fitted F 1s region taken from this work and a number of previous studies are presented in Table S1. In the data sets included, the F 1s spectra were fitted with either one or two components. Below a brief discussion is presented of these data sets assessing their quality, quality of curve fitting, general differences between data sets and other relevent comments. Note that only a limited number of sources are available for which a reasonable signal to noise level in the F 1s spectra of FTO has been obtained and spectral analysis performed. This is because few XPS studies of SnO_2 focus on the dopant, primarily due to the fact that generally low concentrations of fluorine dopant are incorporated into the SnO_2 matrix. Together with the relatively low photoionization cross-section of F 1s compared with many other core level lines, this makes achieving a good signal-to-noise ratio in F 1s spectra a lengthy process (typically taking several tens of hours of scanning). We therefore also present prior results on F 1s binding energy values for F-doped TiO_2 as it possesses the same rutile crystal structure and may exhibit similar F doping properties to FTO.

Suffner *et al.*[10] investigated the effects of different fluorine incorporation into the SnO_2

matrix for FTO nanoparticles grown via chemical vapor synthesis. They reported that, as fluorine incorporation is increased, a shoulder component emerges at high binding energy in the F 1*s* spectra. The F 1*s* spectrum was curve fitted with two components, but the report gave no information about the line shapes or the background used to fit the data and so it is difficult to properly judge their analysis and interpretation and compare our F 1*s* data to theirs. A negligible carbon signal is seen in the C 1*s* spectrum, which would usually indicate some form of surface cleaning to get rid of adventitious carbonaceous species. However, no surface preparation prior to XPS measurement is described. The only very weak C 1*s* intensity does however suggest it is unlikely that the F 1*s* shoulder component is the result of C-F bonding associated with atmospheric contamination. No electrical measurements of carrier concentration or mobility are provided for these FTO nanoparticles, making comparisons between their samples and ours difficult. The exact nature of the interstitials suggested by Suffner *et al.* is in contrast to what we see in our DFT results. They proposed the fluorine substitutional-interstitial pair is the most probable defect accounting for the effects seen on the unit cell volume via XRD measurements.

This defect was also suggested by Canestrato *et al.*[19] to account for similar observations of a changing lattice parameter as determined via XRD. We have shown theoretically that this defect has a much higher formation energy for FTO in the degenerate regime and so is less likely to form than interstitial fluorine. Park *et al.*[11] looked at metal-organic CVD-deposited FTO. They showed the Sn 3*d*, C 1*s* and F 1*s* regions for four samples with different tin incorporation rates. The Sn 3*d* spectra show good signal-to-noise ratio, but the peak assignment is incorrect. They claim the $3d_{3/2}$ peak is due to Sn-O bonding and the $3d_{5/2}$ peak is a component due to Sn-F bonding. Obviously this is incorrect, as any chemically shifted contributions to the Sn 3*d* spectra must have both $3d_{5/2}$ and $3d_{3/2}$ components with spin orbit separation of 8.4 eV. Similarly the C 1*s* spectra have also not been fitted but three components are claimed: C-H, C-F and C-O. It is very difficult to see these due to the poor signal-to-noise, and really only an adventitious hydrocarbon carbon peak is obvious at

~284.6 eV. The F 1*s* spectrum also suffers from poor signal-to-noise. Two components are claimed, again with no fit shown, C-F and C_9F. Strangely, they claim to have made F:SnO_2 but make no mention of substitutional fluorine in this spectrum. There is large ambiguity between the components they are claiming in the text and those in their figure labels. For the reasons stated above the reported F 1*s* peak positions are of little significance.

Chantarat *et al.*[12] also observed two peaks in their XPS F1s spectra for FTO and AZO coated FTO films deposited via chemical pyrolysis and subsequent sputtering of AZO. They report a much larger splitting between two F 1*s* components of 2.8 eV. These components are assigned to Sn-F (low binding energy) and C-F (high binding energy). Focusing on the F 1*s* spectra of the FTO (without AZO deposited on top) there is relatively good signal-to-noise in the data. Three spectra are shown corresponding to a number of cleaning processes. Strangely no fluorine is seen in the as deposited or annealed samples. This is in spite of a measured carrier concentration of 5.5×10^{20} cm^{-3}, suggesting significant fluorine content must be present in the as deposited samples. Only the H-plasma cleaned samples display a clear fluorine peak. The fitting of the F 1*s* spectrum is fairly poor, containing an F-Sn component that has a very large full width at half maximum (FWHM) without any justification and a second high binding energy component again with a high FWHM and intensity similar to that of the noise. This component accomodates the asymmetry of the F 1*s* peak, but should probably be shifted to lower binding energy and the FWHM of both peaks constrained to lower, more reasonable values. We suggest such curve fitting would to some extent better correspond to our analysis of our data.

However, it is important to note that none of the curve fitting of the XPS data from heavily doped FTO discussed above included the effects of plasmon loss features. In fact, this feature is more often than not neglected in XPS analysis of TCOs. Generally, no mention is made of the influence of components related to the high density of free carriers on the core level spectral features. Further instances of F 1*s* data not being curve fitted include those of Noor *et al.* and Martinez *et al.*[13,14] These data sets are typical of most in the literature and

provide little information about possible dopant bonding configurations in FTO other than stating a binding energy position of the F 1*s* peak that roughly corresponds to the Sn-F bond. Peak fitting information is rarely provided, making it difficult to assess the validity of the data analysis.

TiO_2 is a material that shares the rutile structure of SnO_2 and allows for fluorine incorporation on an oxygen site much in the same way as tin dioxide. Hence, it is not unreasonable that F-doped TiO_2 *may* share similar doping properties to FTO. In that vein we have also provided a number of examples of XPS analysis focused on the F1s region of F-doped TiO_2. Seo *et al.*[15] achieved high quality F:TiO_2 films through the use of DC magnetron sputtering and subsequent fluorine plasma insertion. The F 1*s* spectra they measure from this material has been fitted using two components, designated Ti-F and interstitial F. Their data set has good signal-to-noise and the fit line agrees well with the experimental data. Broadly, this evidence agrees with the notion that F can act in a similar manner in both SnO_2 and TiO_2 and occupy interstitial sites.

Li *et al.*[16] studied N and F co-doped TiO_2 and found two components to their F 1*s* peak. The signal-to-noise ratio is poor in the F 1*s* spectra and leads to significant ambiguity in the binding energies of the components, with the Ti-F peak reported as having slightly lower energy than expected. They attribute these peaks to substitutional fluorine, and an oxyfluoride component. The oxyfluoride component would be most likely to arise from contamination of the film in air. Much like the carbonaceous fluorine component seen in figure S3, we would expect an oxygen-fluorine bond to have high binding energy.[2] The energy separation between the two components matches well with what our separation between substitutional and interstitial components, and with other reports we have discussed.

Finally, two reports worth mentioning are from Trapalis *et al.*[17] and Czoska et al.[18] who have reported XPS spectra for F:TiO_2 powders produced via the sole-gel method. These materials have the added complexity of existing in both the rutile and anatase phases which may in fact coexist in the powders if the anatase to rutile transformation is not fully made.

This difference in structure may mean F behaves differently when incorporated into the films, and so we will not dwell too much on these studies. However, Czoska *et al.* clearly show two components fitted to a F 1s spectrum: a substitutional component and a component they assign to fluorine substituting a surface hydroxyl group. We see no evidence of OH in our O 1s spectra (Figure 4 of main text) and so this possibility can be ruled out for our data.[20] Trapalis *et al.* showed an asymmetric peak with no fit, but claimed at least three components, a contamination or non-stoichimetric $TiO_{2x}F_x$ component at high binding energy ($\sim$ 688eV), a peak associated with $TiOF_2$ ($\sim$ 685.4eV), and either TiF_4 or physisorbed F on TiO_2 ($\sim$ 684.3eV). Without curve fitting, the validity of these assignments is difficult to assess. However, the binding energy shift reported between components is again similar to that in our FTO F 1s data.

References

(1) Moulder, J. F.; Stickle, W. F.; Sobol, P. E.; Bomben, K. D. In *Handbook of X-ray Photoelectron Spectroscopy*; Chastain, J., King, R., Eds.; Physical Electronics, Division, Perkin-Elmer Corporation: Eden Prairie, Minnesota, USA, 1992; p 261.

(2) Ferraria, A. M.; Lopes da Silva, J. D.; Botelho do Rego, A. M. *Polymer* **2003**, *44*, 7241–7249.

(3) Sleigh, C.; Pijpers, A.; Jaspers, A.; Coussens, B.; Meier, R. J. *Journal of Electron Spectroscopy and Related Phenomena* **1996**, *77*, 41–57.

(4) Baur, W. H. *Acta Crystallographica* **1956**, *9*, 515–520.

(5) Downs, R. T.; Hall-Wallace, M. *American Mineralogist* **2003**, *88*, 247–250.

(6) Bhachu, D. S.; Waugh, M. R.; Zeissler, K.; Branford, W. R.; Parkin, I. P. *Chemistry - A European Journal* **2011**, *17*, 11613–11621.

(7) Thangaraju, B. *Thin Solid Films* **2002**, *402*, 71–78.

(8) Martinez, A. I.; Acosta, D. R. *Thin Solid Films* **2005**, *483*, 107–113.

(9) Amanullah, F.; Pratap, K.; Hari Babu, V. *Materials Science and Engineering: B* **1998**, *52*, 93–98.

(10) Suffner, J.; Ágoston, P.; Kling, J.; Hahn, H. *Journal of Nanoparticle Research* **2010**, *12*, 2579–2588.

(11) Park, J. H.; Byun, D. J.; Lee, J. K. *Journal of Electroceramics* **2009**, *23*, 506–511.

(12) Chantarat, N.; Hsu, S.-H.; Lin, C.-C.; Chiang, M.-C.; Chen, S.-Y. *Journal of Materials Chemistry* **2012**, *22*, 8005–8012.

(13) Noor, N.; Parkin, I. P. *J. Mater. Chem. C* **2013**, *1*, 984–996.

(14) Martínez, A. I.; Huerta, L.; de León, J. M. O.-R.; Acosta, D.; Malik, O.; Aguilar, M. *Journal of Physics D: Applied Physics* **2006**, *39*, 5091–5096.

(15) Seo, H.; Baker, L. R.; Hervier, A.; Kim, J.; Whitten, J. L.; Somorjai, G. A. *Nano Letters* **2011**, *11*, 751–756.

(16) Li, X.; Zhang, H.; Zheng, X.; Yin, Z.; Wei, L. *Journal of Environmental Sciences* **2011**, *23*, 1919–1924.

(17) Todorova, N.; Giannakopoulou, T.; Romanos, G.; Vaimakis, T.; Yu, J.; Trapalis, C. *International Journal of Photoenergy* **2008**, 534038.

(18) Czoska, a. M.; Livraghi, S.; Chiesa, M.; Giamello, E.; Agnoli, S.; Granozzi, G.; Finazzi, E.; Valentin, C. D.; Pacchioni, G. *The Journal of Physical Chemistry C* **2008**, *112*, 8951–8956.

(19) Canestraro, C. D.; Oliveira, M. M.; Valaski, R.; da Silva, M. V. S.; David, D. G. F.; Pepe, I.; Silva, a. F. D.; Roman, L. S.; Persson, C. *Applied Surface Science* **2008**, *255*, 1874–1879.

(20) McCafferty, E.; Wightman, J. P.; Mcca, E.; Wightman, J. P. *Surface And Interface Analysis* **1998**, *26*, 549–564.